



Comparing intergranular corrosion in Al-Mg-Si-Cu alloys with and without α -Al(Fe,Mn,Cu)Si particles

Adrian Lervik¹ | Turid Danbolt² | Trond Furu^{2,3} | Randi Holmestad¹ | Otto Lunder^{2,4}

¹Department of Physics, Norwegian University of Science and Technology (NTNU), Trondheim, Norway

²Department of Materials Science and Engineering, Norwegian University of Science and Technology (NTNU), Trondheim, Norway

³Norsk Hydro ASA, Oslo, Norway

⁴SINTEF Industry, Trondheim, Norway

Correspondence

Adrian Lervik, Department of Physics, Norwegian University of Science and Technology (NTNU), N-7491 Trondheim, Norway.

Email: Adrian.lervik@ntnu.no

Funding information

Norges Forskningsråd, Grant/Award Numbers: 197405, 247598

Abstract

In this study, a model alloy without Fe and Mn additions, is compared with a commercial AA6005 alloy to further understand how the α -Al(Fe,Mn,Cu)Si particles affect intergranular corrosion (IGC) behaviour. Both alloys were subjected to an accelerated IGC test for durations ranging from 1 to 120 h. Microstructures were studied using scanning and transmission electron microscopy, and electron backscatter diffraction. The presence of α -Al(Fe,Mn,Cu)Si particles yields significantly more uniform IGC attacks and higher corrosion rates. However, the maximum depth of IGC attacks reaches similar values after ~24 h of exposure. This is attributed to the formation of Cu-rich particles along the grain boundaries during the corrosion process, which further catalyses the cathodic reactions.

KEYWORDS

aluminium alloys, electron microscopy, grain boundaries, intergranular corrosion, microstructure

1 | INTRODUCTION

Extruded Al-Mg-Si-(Cu) (6xxx series) alloys are extensively used in the transportation industry due to their favourable properties such as high strength-to-weight ratio, extrudability and formability.^[1,2] These alloys achieve a significant hardness increase from heat treatments (artificial ageing) due to the formation of nanoscale semicoherent and metastable precipitates. At maximum hardness, the needle-shaped β'' -(Al₂Mg₅Si₄) precipitate, growing along the $\langle 100 \rangle_{\text{Al}}$ directions, is present in high number densities.^[3-5] A small addition of Cu is known to have effects on the age-hardening response and the achievable strength.^[6-13] Cu additions will also alter the

metastable phases that form and develop during the artificial ageing stage.^[5,13,14] With prolonged ageing, Cu incorporates into the nanoscale precipitates and develops them to Q'-(Al₆Mg₆Si₇Cu₂),^[15] or other hybrid structures.^[5,13,16]

A drawback with these alloys, which prevents usage in many applications, is susceptibility to intergranular corrosion (IGC). This is observed in Cu-containing Al-Mg-Si alloys with Mg/Si ratio close to unity and is believed to be associated with elemental segregation of Cu along the grain boundaries, surrounding solute-depleted zones and the presence of grain boundary particles.^[16-23] Electrochemical properties and IGC susceptibility have been studied for numerous alloy compositions subjected to

This is an open access article under the terms of the Creative Commons Attribution License, which permits use, distribution and reproduction in any medium, provided the original work is properly cited.

© 2020 The Authors. *Materials and Corrosion* published by Wiley-VCH GmbH

different thermo-mechanical treatments.^[16,17,20,21,24-29] In general, IGC in aluminium alloys is mostly found in the under- and peak-aged tempers, whereas the over-aged temper usually is dominated by pitting corrosion. However, large variations are reported due to different alloy compositions, variations in quenching- and artificial ageing parameters and mechanical treatments.

Large primary α -Al(Fe,Mn,Cu)Si-phase particles are formed during casting and/or homogenisation through the β to α transformation,^[30-32] and have an effect on the recrystallisation of new grains after the profile exits the forming die. Smaller ($<0.3\ \mu\text{m}$) α -Al(Fe,Mn,Cu)Si dispersoids are also formed during these stages by preferential nucleation on the β' particles.^[33-36] Larsen et al.^[19] demonstrated that by removing these primary particles from the surface, by etching the samples in fluonitric acid, significantly less IGC was present as compared to the case where the particles were still present on the surface. It was demonstrated by Kumari et al.^[23] that IGC in an AA6005 alloy initiated at the α -Al(Fe,Mn,Cu)Si particles present at the surface. The α -Al(Fe,Mn,Cu)Si particles dissolved rapidly in an acidified NaCl solution commonly used in assessing IGC susceptibility.^[23,37] Due to selective corrosion, Cu was found to enrich on the outer surfaces causing increased cathodic activity with increased time of immersion.^[23] Selective dissolution of particles where the nobler elements remain has been reported in other Cu-containing intermetallic phases^[38-42] and in other phases found in aluminium alloys.^[41,43-46]

The purpose of this study is to further elucidate the role of α -Al(Fe,Mn,Cu)Si particles in the initiation and propagation of IGC. This is done by comparing two AA6005 alloys, with and without Fe and Mn additions, wherein the latter no α -Al(Fe,Mn,Cu)Si particles are present in the microstructure.

2 | MATERIALS AND METHODS

2.1 | Materials

Two variants of the AA6005 alloy were used in this study. A “model alloy” with only trace amounts of Mn and Fe was provided by American Elements, while the reference alloy is a commercial alloy provided by Hydro (further referred to as “AA6005”). The composition of the two alloys is given in Table 1. Note that the Si content in the model alloy is slightly lower to compensate for the Si which normally would be incorporated into the α -Al(Fe,Mn,Cu)Si primary constituents. The Si content was estimated using the Alstruc homogenisation model.^[47]

The model alloy was homogenised at 550°C for 30 min and subsequently water-quenched. The billet was preheated to 480°C and extruded into a flat profile with 3-mm wall thickness and 65-mm width at a ram speed of 5 mm/s with a following water-quench. Artificial ageing was performed in a Nabetherm N15/65 air circulation furnace at 185°C for 5 h to reach peak hardness (T6). The AA6005 alloy was produced in a similar manner, with the only difference being that the homogenisation was conducted at 585°C for 2.5 h due to a larger billet size.

2.2 | Corrosion testing

Samples with an exposed area of $20 \times 30\ \text{mm}^2$ were IGC tested based on the accelerated standard test “ISO 11846 Method B”. Before IGC testing, the samples were degreased in acetone and etched in 7.5 wt% NaOH solution at 50–60°C for 2.5 min, rinsed and desmutted in 68% concentrated HNO₃ solution for 2 min, then rinsed again in distilled water and air-dried. IGC testing was performed by immersing in a solution of 10 ml/L HCl and 30 g/L NaCl (further referred to as “test solution”), with a ratio of 5-ml-solution per cm² sample area. Immersion times were varied from 1 to 120 h and three samples were tested in parallel for each exposure time. Corrosion products were subsequently removed in a concentrated HNO₃ solution. The samples were weighed before and after the accelerated test. The visible results from the corrosion tests were examined on the cross-section parallel to the extrusion direction using optical microscopy and on the corroded surfaces using scanning electron microscopy (SEM).

2.3 | Electrochemical testing

Cathodic polarisation curves were acquired in the same test solution as in the accelerated IGC ISO standard test. Samples with a surface area of approximately 1 cm² were polished to a mirror finish before they were pre-exposed for 5 min or 5 h in the solution before polarisation at a sweep rate of 1 mV/s, starting at the open-circuit potential.

TABLE 1 Composition of the investigated alloys in at% measured using optical emission spectroscopy

| | Cu | Fe | Mg | Mn | Si | Al |
|-------------|------|------|------|-------|------|------|
| AA6005 | 0.06 | 0.09 | 0.63 | 0.07 | 0.61 | Bal. |
| Model alloy | 0.05 | 0.01 | 0.59 | <0.01 | 0.56 | Bal. |

2.4 | Electron microscopy

Samples for SEM were initially ground using SiC abrasive paper. Subsequent polishing was done using 1- and 0.25- μm diamond spray and for electron backscatter diffraction (EBSD), the samples were vibropolished as the final step. EBSD was performed on a Hitachi SU-6600 FEG-SEM operated at 20 kV. Nordif3.0 was used to index the acquired patterns and the data were subsequently analysed in the open-source MATLAB plugin MTEX.^[48] Backscattered electron (BSE)-SEM images were acquired on a Zeiss Supra 55-VP FEG-SEM operated at 10 kV.

Transmission electron microscopy (TEM) specimens were prepared by grinding bulk specimens with SiC abrasive paper to $\sim 100\text{-}\mu\text{m}$ thickness, punched into 3-mm discs and thereafter electropolished in an electrolyte consisting of one-third HNO_3 and two-thirds CH_3OH at temperatures between -30 and -20°C at 20 V. Two TEM instruments were used in this study. (i) A Cs-corrected JEOL ARM200CF operated at 200 kV with convergence semiangle of 28- and 48-mrad inner collector angle for a high-resolution high-angle annular dark-field (HAADF)-scanning transmission electron microscopy (STEM) imaging. (ii) A JEOL JEM-2100F operated at 200 kV in analytical STEM mode with a 1.0-nm probe size, equipped with an Oxford X-max 80 detector with a solid angle of 0.23 sr for energy-dispersive X-ray spectroscopy (EDS). Some high-resolution STEM images were acquired using Smart Align.^[49]

3 | RESULTS

3.1 | Microstructure

Figure 1 shows representative BSE-SEM images of the microstructure in both alloys, acquired using the same magnification and experimental conditions. In

the AA6005 alloy in Figure 1a, there are particles present with an area coverage of $\sim 0.65\%$ composed of Al, Fe, Mn, Cu and Si as determined by EDS. These are the Fe-rich $\alpha\text{-Al(Fe,Mn,Cu)Si}$ primary constituents. In the model alloy shown in Figure 1b, only a limited amount of particles are present. The few bright regions present are undissolved Si-rich Mg-Si eutectic particles. In both alloys, the dark spots are either Mg_2Si particles or pores.

EBSD was performed on the cross-section of the material covering a region from the surface and into the material. This is shown for the AA6005 and the model alloy in Figures 2a and 2b, respectively. The grains are colour-coded according to the inverse pole figure shown in Figure 2b and the grain boundaries are marked according to their misorientation angle. In the AA6005 alloy, a surface layer with larger grains extending approximately $450\text{ }\mu\text{m}$ into the material is present, before reaching the interior region composed of smaller grains. Figure 2c,d show the normalised grain boundary misorientation angle from the surface ($450\text{ }\mu\text{m}$) and in the interior, for the AA6005 and model alloys, respectively. The fraction of high-angle grain boundaries is greater in the surface layer. The distribution is compatible between the alloys. Due to the absence of the grain size controlling particles, the texture is slightly different in the two materials, where the model alloy exhibits larger grains and more uniform distribution, as demonstrated by Figures 1 and 2.

Precipitate microstructures are found to be similar in the two alloys, as demonstrated in Figure 3 where a bright field (BF)-TEM image and typical HAADF-STEM images of common precipitate structures are shown. The precipitates are mostly the β'' -phase with some Cu inclusions, both in the precipitate and on its interface. This is deduced based on the high Z-contrast of the Cu-containing atomic columns and the formation of the distinguishable Q' -phase subunit.^[14,15]

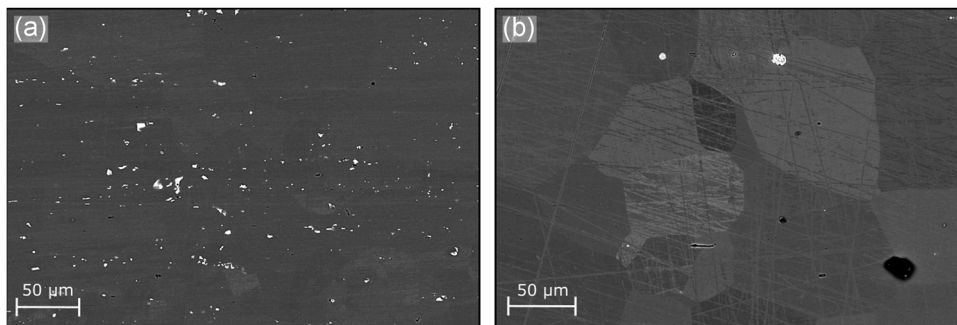


FIGURE 1 Backscattered electron-scanning electron microscopy images acquired at similar magnification for the AA6005 alloy in (a) and the model alloy in (b). The AA6005 alloy contains $\alpha\text{-Al(Fe,Mn,Cu)Si}$ primary particles, which are the bright particles seen in (a). Dark spots observed in both alloys are either Mg_2Si particles or pores

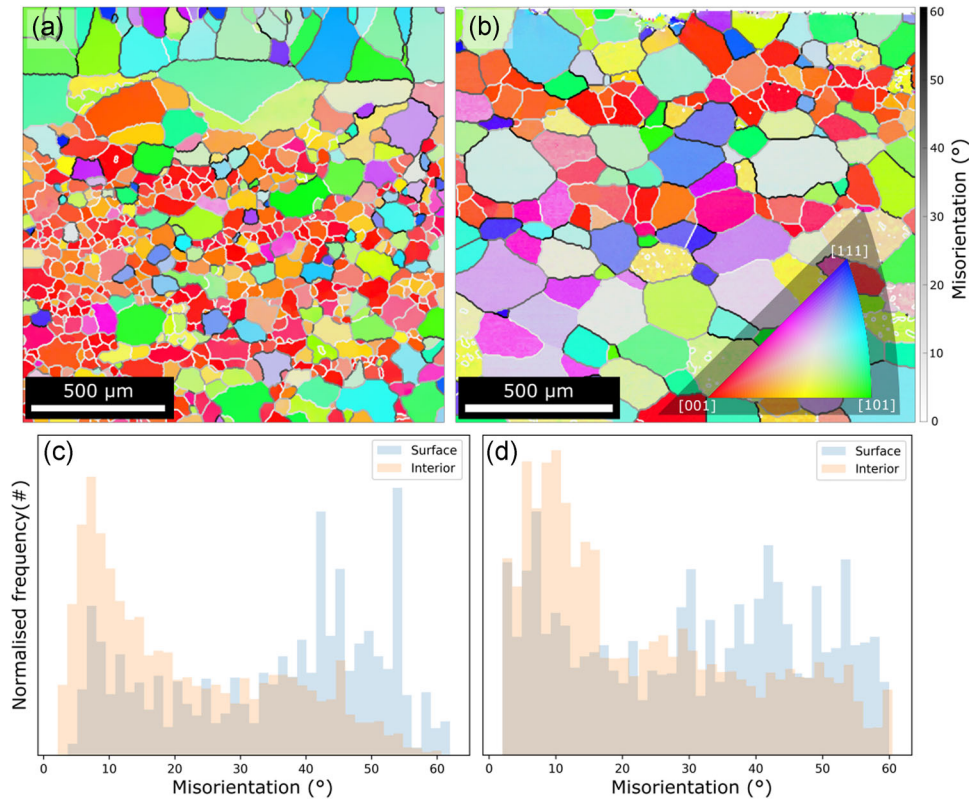


FIGURE 2 Electron backscatter diffraction images acquired on the cross-sections of AA6005 and the model alloy in (a) and (b), respectively. The outer surface is the upper part of both figures. Grains are coloured according to the inverse pole figure in (b), and grain boundaries are colour-coded according to their misorientation. (c, d) Grain boundary misorientation angle for the AA6005 and model alloys, separated into the surface (first 450 μm) and the interior [Color figure can be viewed at wileyonlinelibrary.com]

3.2 | Grain boundaries

A range of grain boundaries appearing both with and without particles was studied using STEM-EDS. An example from the model alloy is shown in Figure 4, where two segments of the same grain boundary can be seen in BF-STEM. They are defined by a similar misorientation angle of $\sim 26^\circ$ between the adjacent $[110]_{\text{Al}}$ and $[130]_{\text{Al}}$ oriented grains. These two segments are separated by a kink, most likely caused by a grain boundary-pinning particle, and demonstrate very different behaviours; one part has continuous precipitation of Q/Q'-phase particles, and in the other part, no particles are present. The upper segment is likely to have a more energetically favourable grain boundary interface plane facilitating for particle nucleation and does not demonstrate any clear indication of elemental segregation between the particles, whereas the lower segment does show segregation of Mg, Cu, and Si, as can be seen in the corresponding EDS maps.

Figure 5 shows a typical low-angle grain boundary in the AA6005 alloy. The adjacent grains are both oriented along the $[100]_{\text{Al}}$ axis. This is nearly a pure-

tilt boundary with a twist component of $\sim 3^\circ$ separating the grains from simultaneously aligning parallel to the electron beam. A solute-depleted precipitate-free zone (PFZ) is associated with this grain boundary and has a width of 70 nm, as highlighted in Figure 5b. The grain boundary particles demonstrate clear coherency with at least one of the adjacent grains, which is seen by the defined $[150]_{\text{Al}}$ interface plane. These are metastable particles adapting the Q'-phase, as can be seen in the HAADF-STEM images in Figures 5c,d. All particles on this grain boundary demonstrate this clear coherency. Figure 5e shows the corresponding EDS maps of Al, Cu, Mg and Si. The grain boundary particles on these low-angle grain boundaries are smaller than those found on high-angle grain boundaries, such as the one presented in Figure 4.

PFZ widths were measured by orienting the grain boundary plane parallel to the electron beam and are on average 131 ± 17 and 83 ± 3 nm, for the model and AA6005 alloy, respectively. Apart from the measured PFZ widths, there were no apparent differences in the grain boundary characteristics in the two alloys.

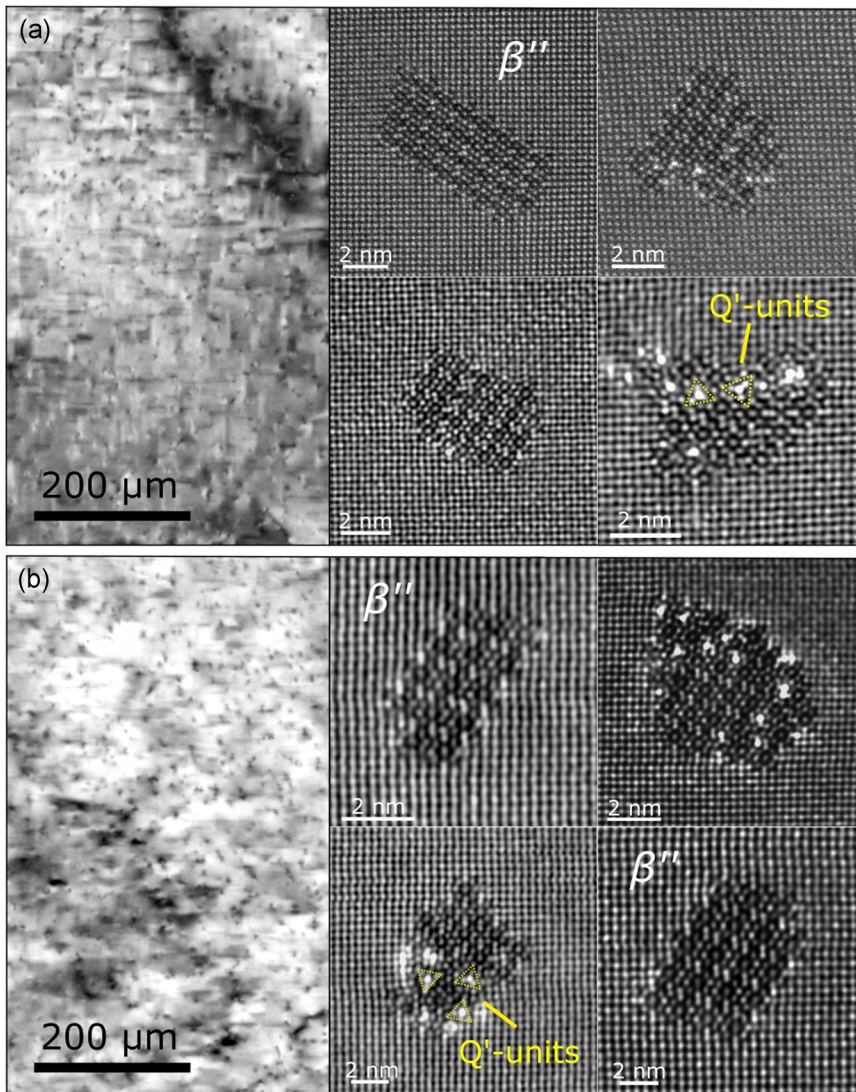


FIGURE 3 Bulk microstructures demonstrated by BF-TEM images acquired along the $[001]_{Al}$ direction for the AA6005 and model alloys in (a) and (b), respectively. Representative HAADF-STEM images of the hardening precipitates are shown and are predominantly β'' with some Cu inclusion on the interface or within the precipitate. (BF-TEM, bright-field-transmission electron microscopy; HAADF-STEM, high-angle annular dark-field-scanning transmission electron microscopy) [Color figure can be viewed at wileyonlinelibrary.com]

3.3 | Corrosion properties

Maximum IGC penetration depth and mass reduction are shown as a function of exposure time to the test solution in Figure 6. Both alloys reach similar values of 400–500 μm for the maximum penetration depths after prolonged exposure. The weight loss is, however, significantly higher in the AA6005 alloy. Low-magnification cross-section images after different exposure times are shown in Figure 7. Less-uniform grain boundary attacks can be seen in the model alloy for all the different exposure times, although the depths are comparable. After 48 h of exposure, entire grains have detached from the surface of the AA6005 alloy.

Figure 8 shows the secondary electron (SE)-SEM images of the corroded surfaces. Nearly all the surface α -particles in the AA6005 alloy were selectively dissolved during the first 5 h of exposure, in accordance with previous observations.^[23,37] AA6005 exhibits only local IGC

attacks after 5 h. After 24 h, these local attacks have developed into a near-continuous network of corroded grain boundaries, where a few grains have detached. At 72 h, only remnants of the original surface are present and the larger subsurface grains, demonstrated in Figure 2, are clearly visible. In the model alloy, only a few, very local, IGC attacks are visible after 5 h of exposure, which develop into localised networks after 24 and 72 h, where large regions are left unaffected in-between. Similar observations regarding the distribution of IGC attacks are made when viewing the cross-section after corrosion testing (cf. Figure 7). In both alloys, corroded grains appear to be etched in a crystallographical manner after 5 h of exposure.

After 24 h in the test solution, particles containing only Cu were observed along the corroded grain boundaries, as demonstrated for the model alloy in Figure 9. EDS mapping of this triple point shows clearly that Cu is associated with bright particles seen in the

FIGURE 4 A grain boundary between two grains oriented along $[110]_{\text{Al}}$ and $[130]_{\text{Al}}$ in the model alloy, demonstrating different precipitation behaviour in the two regions separated by a kink. The upper segment has a continuous distribution of particles, whereas the bottom segment is free of particles [Color figure can be viewed at wileyonlinelibrary.com]

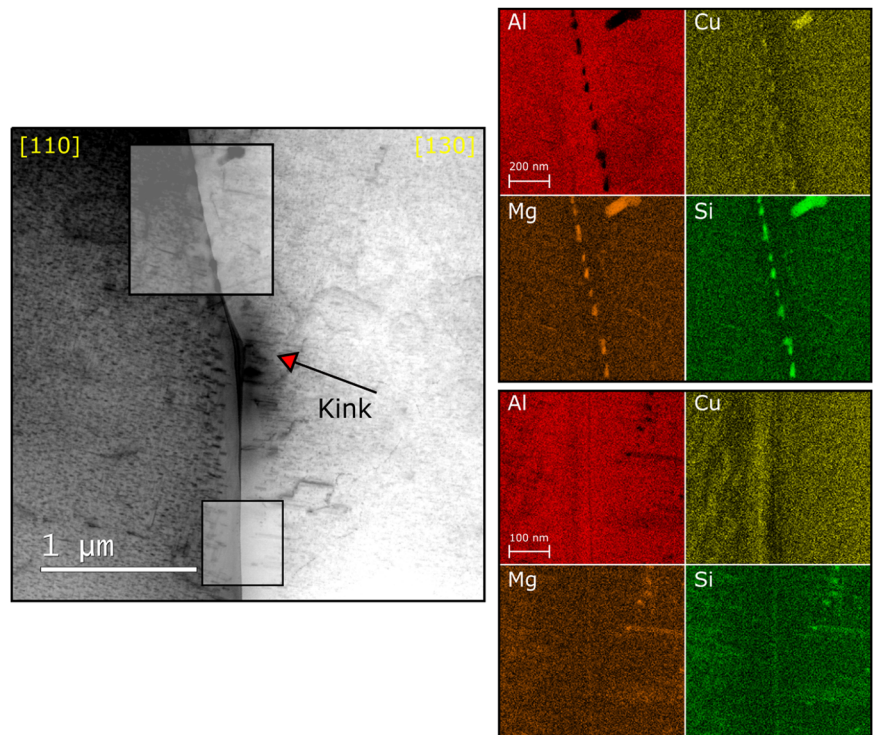


image. EDS spectra acquired from the particle in Figure 9 and from the surrounding grain show that the elements associated with the particle is predominantly Cu, as is clear when comparing with the surrounding matrix

signal. The Al and O signals are likely due to corrosion products found in close proximity to the particle, and not necessarily from the particle itself. Similar observations of Cu-rich particles were also made in the AA6005 alloy.

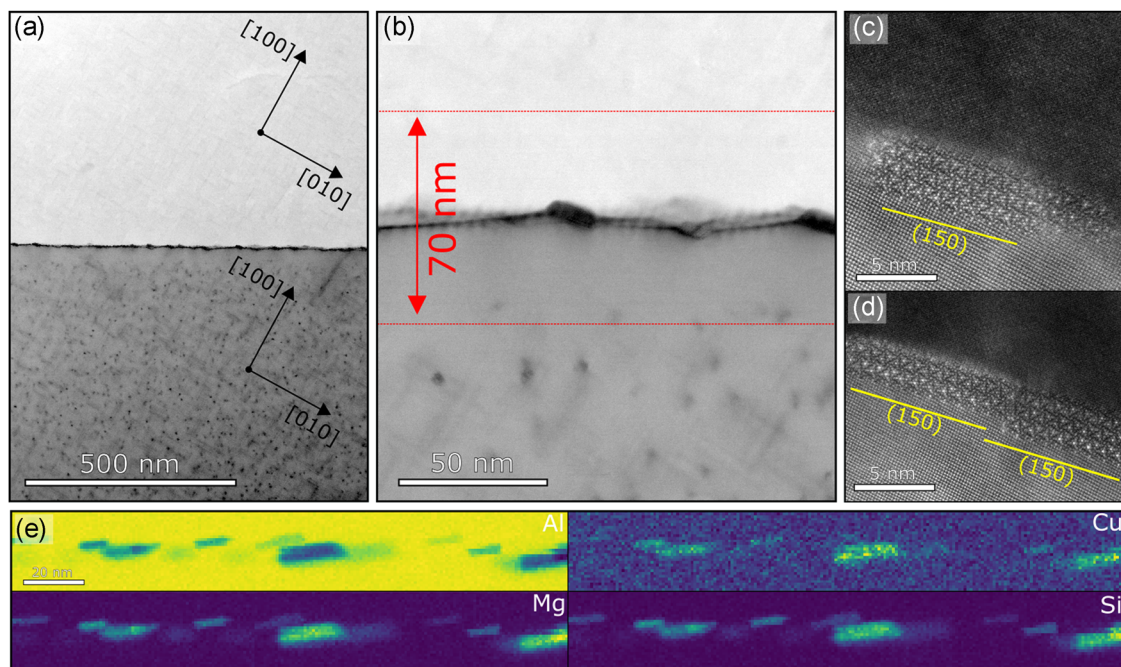


FIGURE 5 A low-angle grain boundary between two $[001]_{\text{Al}}$ oriented grains in the AA6005 alloy demonstrated by two BF-STEM images at different magnifications in (a) and (b). High-resolution HAADF-STEM images of grain boundary Q-phase particles in (c) and (d). Corresponding EDS maps for Al, Cu, Mg and Si in (e). (BF-TEM, bright-field-transmission electron microscopy; EDS, energy-dispersive X-ray spectroscopy; HAADF-STEM, high-angle annular dark-field-scanning transmission electron microscopy) [Color figure can be viewed at wileyonlinelibrary.com]

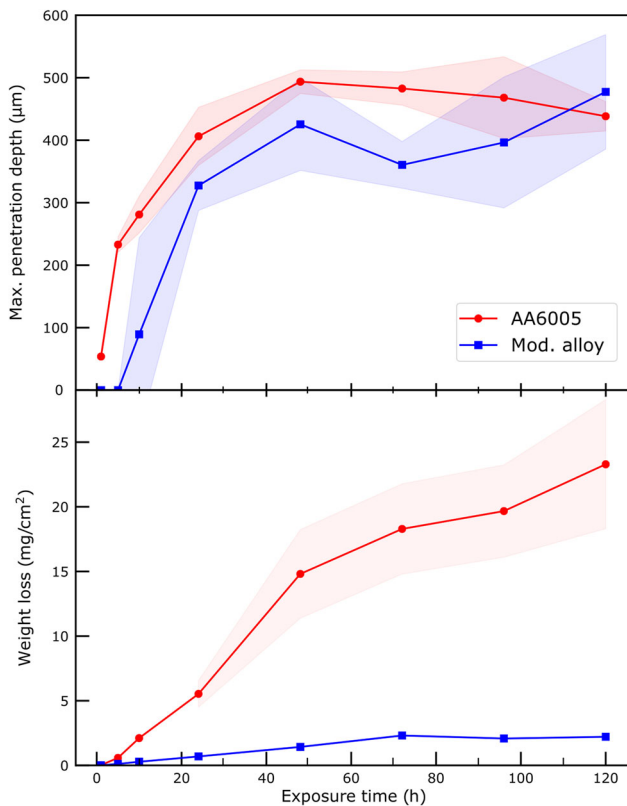


FIGURE 6 Maximum penetration depth (top) and average mass loss (bottom) as a function of exposure time to the accelerated intergranular corrosion test solution for the AA6005 and model alloys. Shaded region represents the standard deviation [Color figure can be viewed at wileyonlinelibrary.com]

3.3.1 | Cathodic polarisation

Cathodic polarisation curves are shown in Figure 10. Conducting the experiment after 5 min of immersion shows that the model alloy has the lowest current density,

approximately one order of magnitude lower than for the AA6005 alloy. Exposing the samples for 5 h in the test solution before polarisation increases the current densities of both alloys and they both exhibit similar values. As the solution has a low pH and is exposed to air, both the oxygen reduction and hydrogen evolution reactions are expected to contribute to the cathodic current density.

4 | DISCUSSION

The present results confirm and supplement previous findings concerning the role of α -Al(Fe,Mn,Cu)Si-phase primary particles in IGC of 6xxx aluminium alloys.^[23,50] The IGC test results shown in Figures 6–8 demonstrate clear differences between the two materials when evaluating according to the ISO standard of 24 h of exposure. The AA6005 alloy had a near-continuous network of corroded grain boundaries, higher weight loss and slightly deeper maximum penetration depth than the model alloy. Only local IGC networks were observed in the model alloy for all exposure durations tested. The reason for this is believed to be due to the lack of initiation sites in the form of α -Al(Fe,Mn,Cu)Si particles in connection to susceptible grain boundaries.^[23,37,50] As a result of the local IGC networks, the weight loss becomes significantly lower in the model alloy than for the AA6005, which exhibits a more uniform distribution of corrosion attacks resulting in the detachment of entire grains, as demonstrated by Figures 7 and 8.

Surface α -Al(Fe,Mn,Cu)Si particles are also likely the reason for the measured difference in the initial cathodic activity for the two alloys, as presented in Figure 10. However, a large increase in cathodic current density was also measured for the model alloy after 5 h of

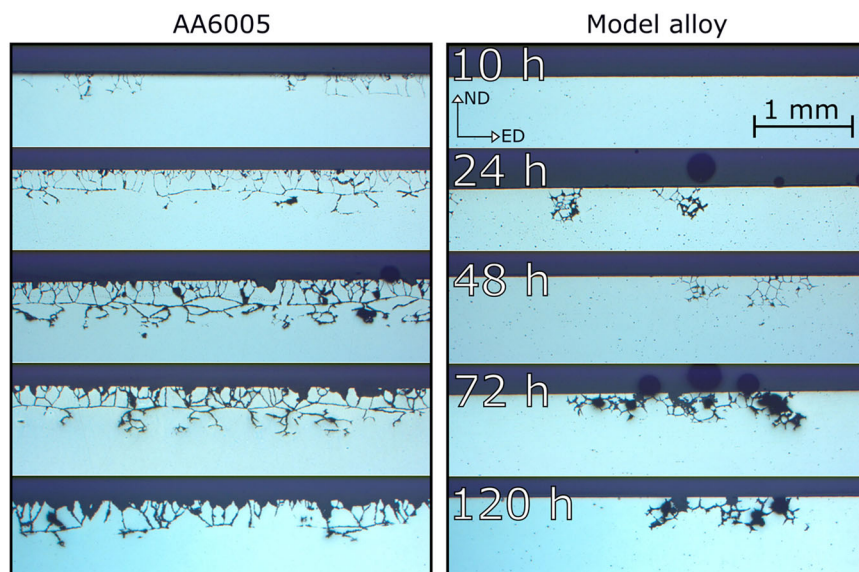


FIGURE 7 Optical microscopy images of the cross-section of the AA6005 and model alloys after 10–120 h of immersion in the accelerated intergranular corrosion test solution [Color figure can be viewed at wileyonlinelibrary.com]

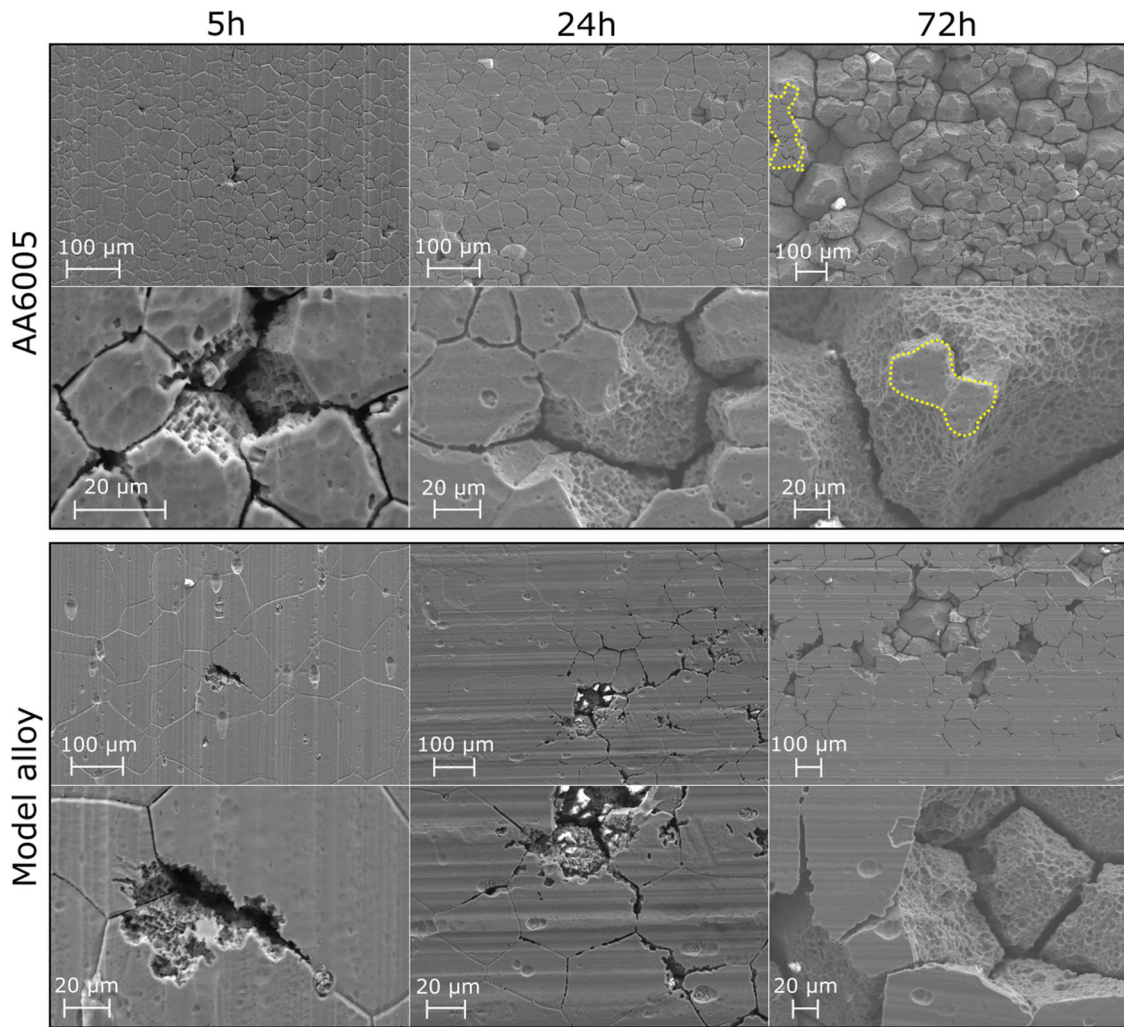


FIGURE 8 Secondary electron-scanning electron microscopy images of the corroded surface after 5, 24 and 72 h of immersion in the accelerated intergranular corrosion test solution for the AA6005 alloy and the model alloy. Yellow dotted lines indicate the original surface, which is barely visible after 72 h of exposure in the AA6005 alloy [Color figure can be viewed at wileyonlinelibrary.com]

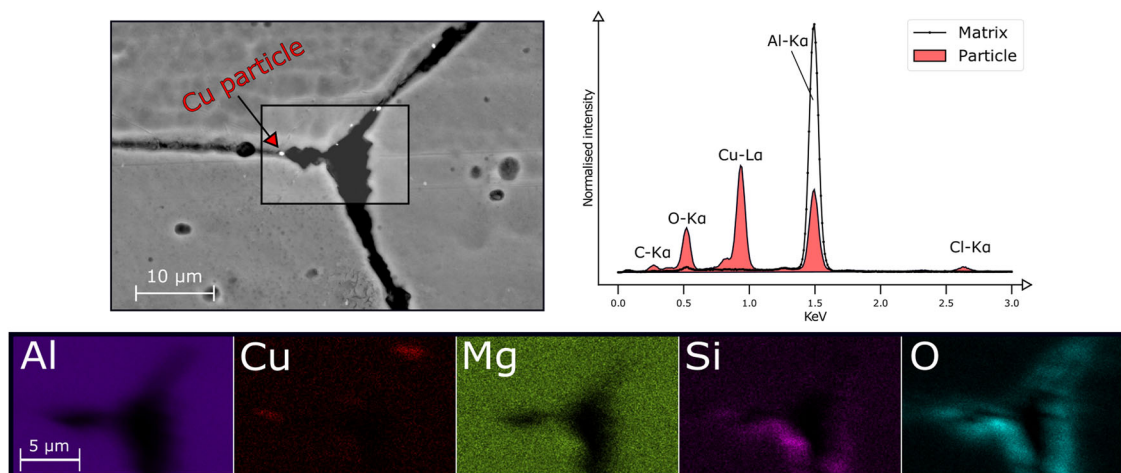


FIGURE 9 A BSE-SEM image of a corroded triple point in the model alloy after 24 h of immersion in the test solution. The bright particles are Cu-rich particles, as shown in the EDS spectrum and the corresponding elemental maps. (BSE-SEM, backscattered electron-scanning electron microscopy; EDS, energy-dispersive X-ray spectroscopy) [Color figure can be viewed at wileyonlinelibrary.com]

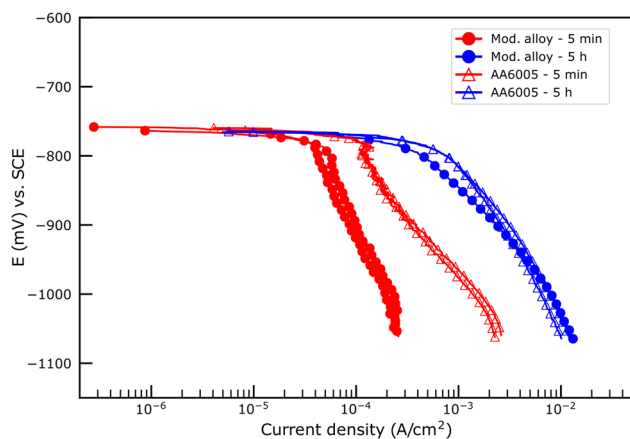


FIGURE 10 Cathodic polarisation curves for the two alloys after 5 min or 5 h of immersion in the test solution before the scan. The current density reaches similar values for both alloys after 5 h of immersion in the test solution [Color figure can be viewed at wileyonlinelibrary.com]

exposure to the test solution. Figures 4 and 5 show that the grain boundaries initially have significant amounts of the Cu-containing Q/Q'-phase particles present. The Q-phase has been demonstrated as a more noble particle than bulk aluminium, although it undergoes selective dissolution leaving behind Cu-rich particles.^[40,42] As such, the increased cathodic activity in the model alloy may be caused by the selective dissolution of such particles, as Cu-remnants were found on several grain boundaries, as exemplified by Figure 9. Cu-rich remnants along corroded grain boundaries have previously been shown by others.^[20,21,50] Understanding the dissolution kinetics of Q-phase particles along grain boundaries and their effect on IGC compared to continuously segregated Cu is considered to be an important fundamental issue, which should be investigated in future work. Furthermore, enrichment of Cu over the entire exposed surface due to uniform dealloying of the Al matrix is also likely to contribute to the enhanced cathodic activity.^[50] The observation that the current density reaches similar values for both alloys is a strong indication that Cu has important roles both as internal and external cathodes.

As demonstrated in Figure 4, a grain boundary defined only by its misorientation angle may have different precipitation behaviour and thus different electrochemical nature. It is likely that certain grain boundary termination planes facilitate preferential particle nucleation. This has been demonstrated in the Al-Zn-Mg alloy system for the MgZn₂ grain boundary particles.^[51] A more comprehensive study correlating grain boundary precipitation, texture, and corrosion properties is suggested as a future study.

Producing alloys free of α -Al(Fe,Mn,Cu)Si particles will not be practical in industry, as Fe is always present

in primary aluminium and the particles are required to control grain size. It is more likely that a surface treatment to remove the surface particles may be applied for components prone to IGC.^[19]

5 | CONCLUSIONS

In this study, the effect of α -Al(Fe,Mn,Cu)Si-phase particles on IGC has been investigated by comparing two alloys. The most important findings are:

- α -Al(Fe,Mn,Cu)Si-phase particles play a key role in the initiation and distribution of IGC. The absence of the surface particles results in fewer, more locally corroded grain boundaries. However, the depth of the corrosion attacks reaches similar values regardless of the initial surface conditions.
- The initial cathodic activity on AA6005 is controlled by the presence of α -Al(Fe,Mn,Cu)Si particles on the surface. Their importance as external cathodes for the propagation of IGC is gradually reduced as the particles dissolve in the accelerated IGC test solution.
- With increasing time of immersion in the test solution, the cathodic activity increases considerably due to surface remnants of Cu, which become the dominating external cathodes.
- Cu-rich remnants originating from grain boundary particles and/or grain boundary segregation decorate the corroded grain boundary and function as internal cathodes.

ACKNOWLEDGEMENTS


John Erik Lein (SINTEF Industry) is gratefully acknowledged for the polarisation measurements. The (S)TEM work was conducted on the NORTEM (NFR: 197405) infrastructure at the TEM Gemini Centre in Trondheim, Norway. This study was supported by the KPN project "FICAL" (NFR: 247598), cofinanced by The Research Council of Norway (NFR), and the industrial partners Norsk Hydro ASA, Gränges, Benteler Automotive Raufoss AS and Steertec Raufoss.

DATA AVAILABILITY STATEMENT

The data that support the findings of this study are available from the corresponding author upon reasonable request.

ORCID

Adrian Lervik  <http://orcid.org/0000-0001-9820-245X>

Randi Holmestad  <https://orcid.org/0000-0002-4274-5794>

REFERENCES

- [1] O. Reiso, *Mater. Forum* **2004**, 28, 32.

- [2] J. Hirsch, *Trans. Nonferrous Met. Soc. China (English Ed.)* **2014**, *24*, 1995.
- [3] S. J. Andersen, H. W. Zandbergen, J. Jansen, C. Træholt, U. Tundal, O. Reiso, *Acta Mater.* **1998**, *46*, 3283.
- [4] H. S. Hasting, A. G. Frøseth, S. J. Andersen, R. Vissers, J. C. Walmsley, C. D. Marioara, F. Danoix, W. Lefebvre, R. Holmestad, *J. Appl. Phys.* **2009**, *106*, 123527.
- [5] J. K. Sunde, C. D. Marioara, A. T. J. van Helvoort, R. Holmestad, *Mater. Charact.* **2018**, *142*, 458.
- [6] W. F. Miao, D. E. Laughlin, *Metall. Mater. Trans. A* **2000**, *31*, 361.
- [7] M. Murayama, K. Hono, W. Miao, D. E. Laughlin, *Metall. Mater. Trans. A* **2001**, *32*, 239.
- [8] J. Man, L. Jing, S. G. Jie, *J. Alloys Compd.* **2007**, *437*, 146.
- [9] C. D. Marioara, S. J. Andersen, T. N. Stene, H. Hasting, J. Walmsley, A. T. J. van Helvoort, R. Holmestad, *Philos. Mag.* **2007**, *87*, 3385.
- [10] T. Saito, C. D. Marioara, J. Røyset, K. Marthinsen, R. Holmestad, *Mater. Sci. Eng. A* **2014**, *609*, 72.
- [11] M. W. Zandbergen, A. Cerezo, G. D. W. Smith, *Acta Mater.* **2015**, *101*, 149.
- [12] Q. Xiao, H. Liu, D. Yi, D. Yin, Y. Chen, Y. Zhang, B. Wang, *J. Alloys Compd.* **2017**, *695*, 1005.
- [13] J. K. Sunde, C. D. Marioara, R. Holmestad, *Mater. Charact.* **2020**, *160*, 110087.
- [14] T. Saito, E. A. Mørtzell, S. Wenner, C. D. Marioara, S. J. Andersen, J. Friis, K. Matsuda, R. Holmestad, *Adv. Eng. Mater.* **2018**, *20*, 1800125.
- [15] S. Wenner, L. Jones, C. D. Marioara, R. Holmestad, *Micron* **2017**, *96*, 103.
- [16] C. D. Marioara, A. Lervik, J. Grønvold, O. Lunder, S. Wenner, T. Furu, R. Holmestad, *Metall. Mater. Trans. A* **2018**, *49*, 5146.
- [17] G. Svenningsen, M. H. Larsen, J. C. Walmsley, J. H. Nordlien, K. Nisancioglu, *Corros. Sci.* **2006**, *48*, 1528.
- [18] M. H. Larsen, J. C. Walmsley, O. Lunder, R. H. Mathiesen, K. Nisancioglu, *J. Electrochem. Soc.* **2008**, *155*, C550.
- [19] M. H. Larsen, J. C. Walmsley, O. Lunder, K. Nisancioglu, *J. Electrochem. Soc.* **2010**, *157*, C61.
- [20] D. Zander, C. Schnatterer, C. Altenbach, V. Chaineux, *Mater. Des.* **2015**, *83*, 49.
- [21] C. Schnatterer, D. Zander, *Surf. Interface Anal.* **2016**, *48*, 750.
- [22] S. K. Kairy, T. Alam, P. A. Rometsch, C. H. J. Davies, R. Banerjee, N. Birbilis, *Metall. Mater. Trans. A* **2016**, *47*, 985.
- [23] S. Kumari, S. Wenner, J. C. Walmsley, O. Lunder, K. Nisancioglu, *J. Electrochem. Soc.* **2019**, *166*, C3114.
- [24] G. Svenningsen, J. E. Lein, A. Bjørgum, J. H. Nordlien, Y. Yu, K. Nisancioglu, *Corros. Sci.* **2006**, *48*, 226.
- [25] G. Svenningsen, M. H. Larsen, J. H. Nordlien, K. Nisancioglu, *Corros. Sci.* **2006**, *48*, 3969.
- [26] G. Svenningsen, M. H. Larsen, J. H. Nordlien, K. Nisancioglu, *Corros. Sci.* **2006**, *48*, 258.
- [27] S. K. Kairy, P. A. Rometsch, K. Diao, J. F. Nie, C. H. J. Davies, N. Birbilis, *Electrochim. Acta* **2016**, *190*, 92.
- [28] S. K. Kairy, P. A. Rometsch, C. H. J. Davies, N. Birbilis, *Corrosion* **2017**, *9312*, 1280.
- [29] Y. Zou, Q. Liu, Z. Jia, Y. Xing, L. Ding, X. Wang, *Appl. Surf. Sci.* **2017**, *405*, 489.
- [30] S. Zajac, B. Hutchinson, A. Johansson, L.-O. Gullman, *Mater. Sci. Technol.* **1994**, *10*, 323.
- [31] H. Tanihata, T. Sugawara, K. Matsuda, S. Ikeno, *J. Mater. Sci.* **1999**, *34*, 1205.
- [32] N. C. W. Kuijpers, F. J. Vermolen, K. Vuik, S. van der Zwaag, *Mater. Trans.* **2003**, *44*, 1448.
- [33] L. Lodgaard, N. Ryum, *Mater. Sci. Forum* **2000**, *331–337*, 945.
- [34] L. Lodgaard, N. Ryum, *Mater. Sci. Eng. A* **2000**, *283*, 144.
- [35] R. Hu, T. Ogura, H. Tezuka, T. Sato, Q. Liu, *J. Mater. Sci. Technol.* **2010**, *26*, 237.
- [36] N. Bayat, T. Carlberg, M. Cieslar, *J. Alloys Compd.* **2017**, *725*, 504.
- [37] K. Shimizu, K. Nisancioglu, *ECS Electrochem. Lett.* **2014**, *3*, C29.
- [38] S. Lebouil, J. Tardelli, E. Rocca, P. Volovitch, K. Ogle, *Mater. Corros.* **2014**, *65*, 416.
- [39] S.-S. Wang, I.-W. Huang, L. Yang, J.-T. Jiang, J.-F. Chen, S.-L. Dai, D. N. Seidman, G. S. Frankel, L. Zhen, *J. Electrochem. Soc.* **2015**, *162*, C150.
- [40] S. K. Kairy, P. A. Rometsch, C. H. J. Davies, N. Birbilis, *Corrosion* **2017**, *73*, 1.
- [41] Y. Zhu, K. Sun, G. S. Frankel, *J. Electrochem. Soc.* **2018**, *165*, C807.
- [42] A. I. Ikeuba, B. Zhang, J. Wang, E. H. Han, W. Ke, *Appl. Surf. Sci.* **2019**, *490*, 535.
- [43] K. Nisancioglu, *J. Electrochem. Soc.* **1990**, *137*, 69.
- [44] N. Birbilis, R. G. Buchheit, *J. Electrochem. Soc.* **2005**, *152*, B140.
- [45] N. Birbilis, R. G. Buchheit, *J. Electrochem. Soc.* **2008**, *155*, C117.
- [46] J. Li, J. Dang, *Metals* **2017**, *7*, 84.
- [47] A. L. Dons, *J. Light Metals* **2001**, *1*, 133.
- [48] F. Bachmann, R. Hielscher, H. Schaeben, *Solid State Phenom.*, Vol. **160**, **2010**, pp. 63–68.
- [49] L. Jones, H. Yang, T. J. Pennycook, M. S. J. Marshall, S. van Aert, N. D. Browning, M. R. Castell, P. D. Nellist, *Adv. Struct. Chem. Imaging* **2015**, *1*, 8.
- [50] S. Kumari, S. Wenner, J. C. Walmsley, O. Lunder, K. Nisancioglu, *Corros. Sci.* **2019**, *158*, 108090.
- [51] H. Löffler, P. Czurratis, R. Kroggel, *Czechoslovak J. Phys. B* **1988**, *38*, 444.

How to cite this article: Lervik A, Danbolt T, Furu T, Holmestad R, Lunder O. Comparing intergranular corrosion in Al-Mg-Si-Cu alloys with and without α -Al(Fe,Mn,Cu)Si particles. *Materials and Corrosion*. 2020;1–10.
<https://doi.org/10.1002/maco.202011954>